



# Transformation- and twinning-induced plasticity in phase-separated bcc Nb-Zr alloys: an atomistic study

Md Mahmudul Hasan<sup>1</sup>, Srivilliputhur G. Srinivasan<sup>2</sup>, and Deep Choudhuri<sup>1,\*</sup>

<sup>1</sup> Department of Materials and Metallurgical Engineering, New Mexico Institute of Mining and Technology, Socorro, NM 87801, USA

<sup>2</sup> Department of Materials Science and Engineering, University of North Texas, Denton, TX 76207, USA

**Received:** 3 August 2023  
**Accepted:** 22 October 2023  
**Published online:**  
17 November 2023

© The Author(s), 2023

## ABSTRACT

Several high-temperature body-centered cubic (bcc) structural materials such as Nb-, Zr- and Ti-based alloys undergo phase separation, which is a second-order phase transformation, whereby the host lattice decomposes into distinct bcc domains with different compositions. Using atomistic simulations, we studied the high-strain-rate response of bcc-forming Nb-*x*Zr (*x* = 0, 25, 50 at.%) alloys. To induce phase separation in our starter alloy, we first employed hybrid Monte Carlo/Molecular Dynamics simulations in single crystals of Nb-*x*Zr at 1000 K. Subsequently, these crystals were deformed along different crystallographic orientations ( $\langle 001 \rangle$ ,  $\langle 110 \rangle$  and  $\langle 111 \rangle$ ) at a strain rate of  $10^{+8} \text{ s}^{-1}$ , to investigate orientation dependent mechanical response. The phase-separated Nb-*x*Zr microstructures exhibited distinct bcc domains enriched in either Zr or Nb. Notably, Nb-50 at.%Zr contained coarser Zr-domains compared to Nb-25 at.%Zr. The Zr-rich domains acted as “soft” inclusions, resulting in reduced peak strengths in the following order: pure Nb (Nb-0 at.%Zr) > Nb-25 at.%Zr > Nb-50 at.%Zr. This implies that phase separation causes softening in Nb-*x*Zr. We also discovered two deformation pathways that depended on the crystallographic orientation: (i) For deformation along  $\langle 110 \rangle$  and  $\langle 111 \rangle$  directions: Elastic deformation was followed by dislocation plasticity on  $\{110\}\langle 111 \rangle$  slip systems; and (ii) For deformation along  $\langle 001 \rangle$  direction: Elastic deformation was followed by the formation of a volumetric fcc structure, twinning on  $\{112\}\langle 111 \rangle$  system, and the formation fcc-phase at the twin/matrix interfacial regions. This was ultimately accompanied by dislocation plasticity on  $\{110\}\langle 111 \rangle$  slip system. The bcc→fcc displacive transformation facilitated  $\{112\}\langle 111 \rangle$  twinning when Nb-*x*Zr was deformed along  $\langle 001 \rangle$ . Our investigation shows that softening of bcc alloys can result from a coupling of mechanisms involving local solute segregation, displacive phase transformation and twinning occurring across multiple slip planes.

Handling Editor: M. Grant Norton.

Address correspondence to E-mail: deep.choudhuri@nmt.edu

## Introduction

Body-centered cubic (bcc) niobium (Nb) is well known for its high melting point and good room-temperature ductility compared to other refractory metals [1]. Alloying Nb with zirconium (Zr) creates alloys with potential applications in nuclear and biomedical technologies [1–3]. Several studies have been conducted on the microstructure and mechanical properties of Nb-rich ( $\leq 1$  at.%Zr, or Zr-lean) and Nb-lean ( $\geq 80$  at.%Zr, or Zr-rich) compositions [4]. Typically, Nb-rich compositions are based on bcc ( $\beta$ -phase, space group  $Im\bar{3}m$ ) crystal structure that forms a single-phase solid solution. However, depending on Zr content, these alloys can form hexagonal closely packed ( $\alpha$ -phase, space group  $P6/mmc$ ), and hexagonal ( $\omega$ -phase, space group  $P6/mmm$ ) structures within the parent-phase. Thus, depending on alloy compositions, Nb-Zr can manifest several types of crystal structures. This study will exclusively focus on bcc-forming Nb-Zr compositions.

Despite such a large body of literature, there remains a knowledge gap in our understanding of Nb-Zr compositions that lie within the miscibility gap of its equilibrium phase diagram, approximately within  $\sim 20$ – $90$  at.%Zr at  $\sim 893$  K [1–6]. In such alloys, phase separation occurs, where the bcc or  $\beta$ -phase decomposes into two bcc domains with different concentrations of Nb or Zr [4, 6]. This process, also known as iso-structural decomposition or phase separation, leads to compositional modulations within the lattice, visible as extra reciprocal lattice reflections in electron diffraction patterns [4, 6–11]. In case of Nb-40 at.%Zr, such reflections are associated with  $[100]$  reflections, which suggested that compositional modulations were along  $\langle 001 \rangle$  [6]. Note that such phase separation tendencies are also seen in many other systems, including  $\beta$ -titanium alloys [4, 10, 11].

The miscibility gap observed in materials like Nb-Zr is attributed to a positive heat of mixing and is significant for achieving homogeneous microstructures [1–3]. Conventional processing methods necessitate long-term annealing at high temperatures, typically between  $\sim 893$  and  $1250$  K, to produce a phase-separated microstructure in Nb-Zr [6]. Unfortunately, this energy-intensive procedure, combined with the high melting points of Zr and Nb, makes it costly and time-consuming. On the contrary, employing atomistic simulations can circumvent such challenges and provide mechanistic insights that are consistent with

experimental results [12–16]. This study aims to investigate the phase separation tendencies in Nb- $x$ Zr ( $x = 0, 25, 50$  at.%) using molecular dynamics simulations and, importantly, evaluate their impact on the mechanical response of such alloys. The results from this investigation are expected to guide materials selection strategies for designing bcc Nb-Zr-based alloys specifically tailored for applications at extreme conditions, such as high temperatures, stresses and strain rates.

Information regarding deformation mechanisms in phase-separated Nb-Zr microstructures is currently limited in the literature. However, existing experimental and computational studies on pure Nb and other bcc metals provide guidance on the anticipated deformation mechanisms, the influence of composition (e.g., on strength) and, notably, deformation-induced phase transformations. In the case of pure Nb, dislocation plasticity is often governed by  $\{110\}\langle 111 \rangle$  slip systems, while twins are known to form on  $\{112\}$  habit planes, oriented along  $\langle 111 \rangle$ , specifically  $\{112\}\langle 111 \rangle$  twinning [17–22]. These observations provide a valuable foundation for understanding potential deformation behaviors in phase-separated Nb-Zr alloys.

The conventional wisdom suggests that the addition of solutes typically strengthens an alloy through solid solution strengthening [17]. However, studies on bcc metals like Mo and W show that a contrary phenomenon where a solute-induced “softening” occurs, which reduces the critical resolved shear stress [23–25]. This softening effect arises from a positive interaction energy between the solute and screw dislocation line segments. Consequently, this interaction enhances the kink pair nucleation, enabling dislocation lines to easily glide through the bcc lattice [24]. In some literature, this phenomenon is also referred to as “double kink” instead of kink pair [17]. Therefore, there is an abiding scientific interest in studying the phase separation effects on the strength of Nb-Zr compositions that lie within the miscibility gap. Thus, understanding the influence of phase separation on the mechanical properties can aid in optimizing the alloy performance.

Lastly, a growing body of experimental work supports the notion that pure Nb undergoes deformation-induced bcc  $\rightarrow$  fcc transformation [26–29]. Furthermore, density functional theory-based first-principles calculations and in situ high-resolution transmission electron microscopy (TEM) suggests that this transformation occurs in proximity to the  $\langle 001 \rangle$  directions [28, 30]. In essence, the crystallographic anisotropy also plays a

role in influencing the bcc→fcc transformation. Again, these findings underscore the complexity of the deformation behavior in pure Nb itself and emphasize the importance of considering crystallographic orientations in understanding such transformations.

Current literature broadly indicates that an interplay between concentration and anisotropy can influence the strength, deformation mechanisms and, very likely, the phase transformation behavior in phase-separated Nb-Zr alloys. To better understand these effects, we have used molecular dynamics (MD) simulations to study the deformation of Nb- $x$ Zr ( $x = 0, 25, 50$  at.%) single crystals along  $\langle 001 \rangle$ ,  $\langle 110 \rangle$  and  $\langle 111 \rangle$  at a temperature of 1000 K and a strain rate of  $10^8 \text{ s}^{-1}$ . This article is organized as follows: Sect. 2 presents the computational methods used, Sect. 3 discusses the results obtained, and in Sect. 4, we rationalize the key observations.

## Computational methods

Molecular dynamics (MD) simulations were performed by using the large-scale atomic/molecular massively parallel simulator (LAMMPS) [31, 32]. The interatomic interactions in the binary Nb-Zr alloy was described using an angular-dependent potential

(ADP) developed by Starikov and Smirnova [33, 34]. This potential was fitted using lattice parameters of bcc, fcc and hcp phases, point defect formation energies, generalized stacking fault energies, Peierls barrier and diffusion coefficients obtained from first-principles calculations. It captures several key thermodynamic and kinetic quantities as a function of composition. Crucially, this ADP captures positive heat of mixing ( $\Delta H_{mix}$ ) within the composition range  $\sim 20 \leq \text{Zr} \leq 90$  at.% [5, 33–36]. The  $\Delta H_{mix}$  is indicative of a miscibility gap [7] present in the Nb-Zr phase diagram from 900–1250 K [5, 6, 35]. Such a gap causes the solute-rich bcc lattice to phase separate into isostructural solute-rich and solute-lean domains upon long-term annealing [4, 6, 7, 37]. Consequently, this ADP potential allowed us to simulate nanoscale Nb-rich and Zr-rich domains, and study their influence on the mechanical response of cubic Nb-Zr alloys at 1000 K. This operating condition is greater than the  $\beta$ -transus temperature of  $\sim 893$  K in Nb-Zr binary phase diagram [4, 6, 7, 37–39].

Simulation boxes containing the atoms were created using the AtomsK code [40]. Figure 1 shows three types of simulation boxes were employed in our study: (i) Body-centered cubic (bcc) single crystals oriented along the  $\langle 001 \rangle$  cubic axes and with an edge length  $\approx 16 \text{ nm}$ ; (ii) bcc single crystals oriented

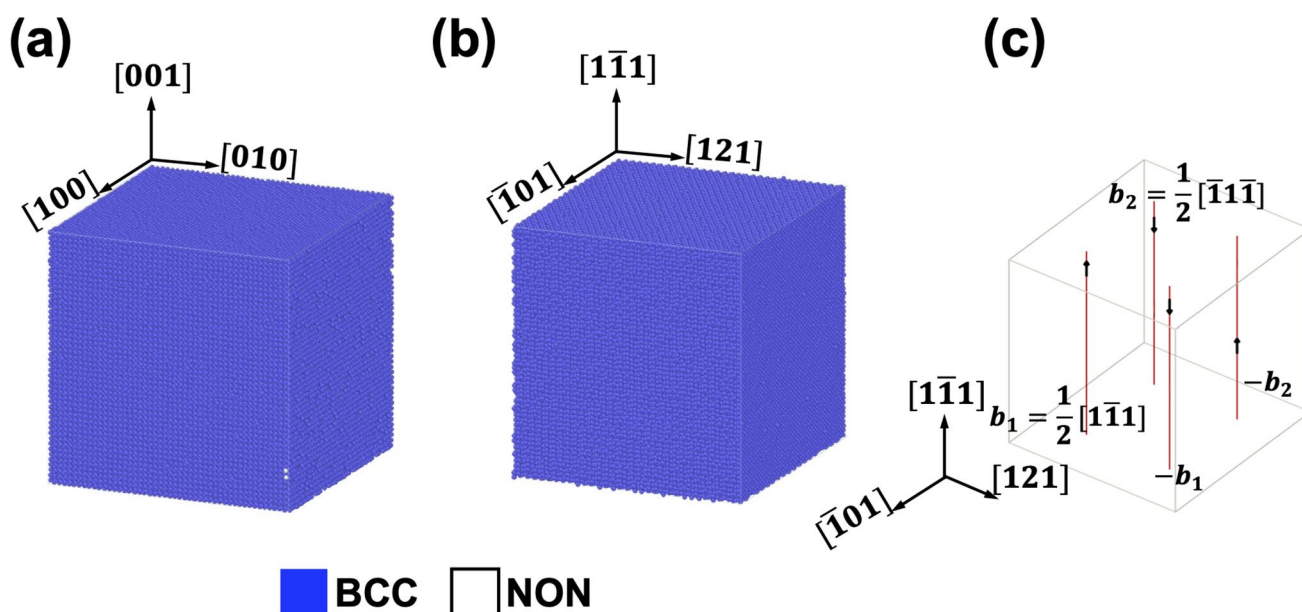


**Figure 1** Geometry of simulation boxes utilized in the study: defect-free single crystals oriented along **a** the  $\langle 100 \rangle$  cube axes, **b**  $[\bar{1}01]$ ,  $[1\bar{1}1]$  and  $[121]$  crystallographic axes of bcc and **d** screw

dislocation quadrupole embedded inside the single crystal with orientations similar to that shown in panel “b”.

along  $[\bar{1}01]$ ,  $[121]$  and  $[1\bar{1}1]$  and an edge length of  $\approx 16$  nm; and (iii) A single crystal containing screw dislocation quadrupole, where the dipole pairs were described by  $\frac{1}{2}[\bar{1}11]$  and  $\frac{1}{2}[1\bar{1}\bar{1}]$  Burgers vectors (Fig. 1d). They were constructed using Volterra displacement fields and equilibrium lattice parameters at the desired composition and temperature [40, 41]. All single-crystal systems contained 211200 atoms.

This work presents the results of three alloys – Nb-0 at.%Zr (pure Nb), Nb-25 at.%Zr and Nb-50 at.%Zr. Note that Nb-25 at.%Zr and Nb-50 at.%Zr lie inside the Nb-Zr miscibility gap [5, 35]. Hybrid Monte Carlo (MC)/MD was employed to achieve the desired compositions. MC steps were performed using the semi-grand canonical ensemble, where the number of particles (N) remain fixed, but the composition can change depending on the chemical potential [42–44]. MD was performed by using a thermostat and barostat to maintain constant number of particles (N), pressure (P) and temperature (T) [42–44]. Therefore, the hybrid MC/MD approach maintains the system under constant N, P and T, but allows compositional changes by imposing different values of the chemical potential difference  $\Delta\mu_{Zr-Nb} = \mu_{Zr} - \mu_{Nb}$ . Following Lei and Hoyt's approach [45], each hybrid MC/MD simulations were initiated using a simulation box containing equiatomic, 50 at.%Nb-50 at.%Zr, composition. In the framework of Metropolis algorithm, this technique assigns each lattice site with equal probability of swapping, and the MC moves drive simulation box toward the desired composition [43]. Prior to carrying out hybrid MC/MD, the randomly substituted structures, including pure Nb structures, were energy-minimized using the conjugate gradient method with force and energy tolerances of  $10^{-6}$  eV and  $10^{-12}$  eV/Å, respectively. Subsequently, all the systems were equilibrated at 1000 K and 0 GPa pressure for 5 million iterations, where 50000 atom swaps were attempted after 10000 MD steps. Extensive testing indicated that  $\Delta\mu_{Zr-Nb} = -0.1, -0.8$  and  $-1.1$  eV yielded 0 (pure Nb), 27.5 and 51.4 at.%Zr. Here, we refer to the Nb-27.5 at.%Zr and Nb-51.4 at.%Zr systems as “25 at.%Zr” and “50 at.%Zr,” respectively. Finally, the hybrid MC/MD-modified undeformed single crystals (Fig. 1a–b) were equilibrated at 1000 K for  $\sim 50$  ps using thermostat and barostat (i.e., NPT ensemble [42–44]) and deformed with a strain rate of  $10^8$  s $^{-1}$  under uniaxial tension. Combined, our computational approach allowed us to examine deformation mechanisms in

phase-separated Nb-Zr at a high temperature of 1000 K and strain rate of  $10^8$  s $^{-1}$ .

MD results were visualized using OVITO [46]. Analysis of dislocation substructures were carried out using the dislocation analysis algorithm (DXA) [47–50]; and the study of local coordination and structure was conducted using the polyhedra template matching algorithm (PTM). These results are shown in Fig. 1a–c [51]. The atomic strain tensors [52] facilitated computing the per-atom von Mises effective strains, which are helpful in characterizing the effect of shear strains on structural changes during deformation [53, 54]. Mathematical formulation for per-atom von Mises effective strain is summarized elsewhere [52, 53]. The PTM algorithm is particularly suited for detecting crystalline structures at higher temperatures, because the identification procedure is not hampered by atomic vibrations [15, 16, 51, 55]. As a result, PTM was employed to separate bcc and face-centered cubic (fcc) coordinated atoms at 1000 K from those belonging to severely distorted regions. A root mean squared deviation (RMSD) value of 0.12 was found to reliably identify all structures.

## Results

The simulation results are presented in three categories. First, we present the undeformed structures at 1000 K, which were obtained using hybrid MC/MD simulations (Sect. 3.1). This section highlights the effect of phase separation within bcc lattice on nanoscale features in single crystals and multi-crystal ensembles. Second, we compare and contrast the stress–strain responses of these structures at 1000 K and  $10^8$  s $^{-1}$  strain rate Sect.3.2). Third, we correlate the observed mechanical responses with the underlying deformation mechanisms (Sects. 3.3 and 3.4).

### Undeformed structures at 1000 K

Figure 2 shows the atomic distribution in Nb- and Zr-rich regions within the undeformed 25 at.%Zr (Fig. 2a) and 50 at.%Zr (Fig. 2b) single crystals, using (100), (011) and (111) planar views. (For comparison, Fig. 2c shows another simulation cell, where bcc sites are randomly substituted by 25 at.%Zr.) In the (100)-view, these Nb- and Zr-rich regions are distributed along two perpendicular  $\{110\}$  planes in the bcc lattices of 25 and 50 at.%Zr, respectively. This arrangement is

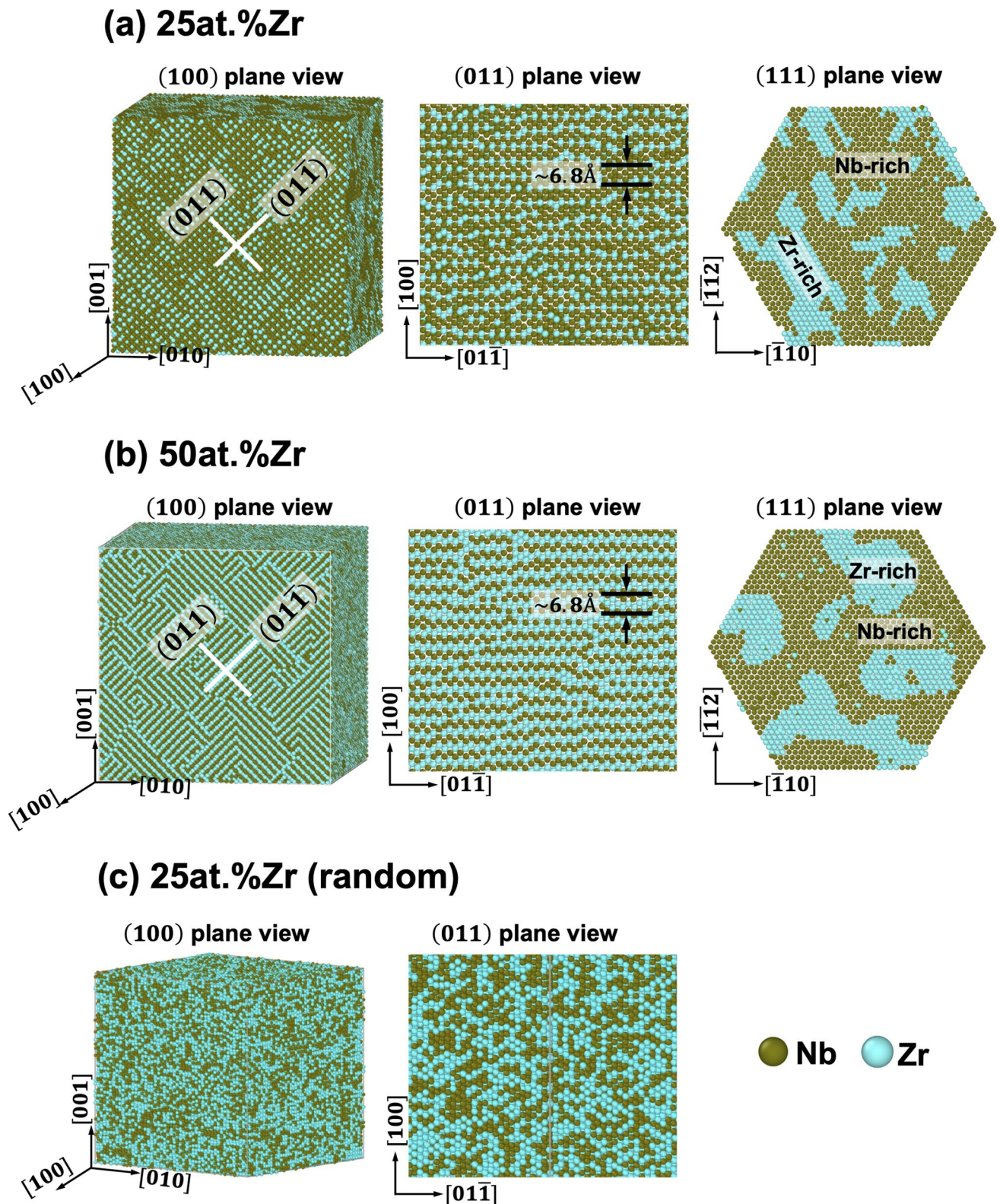


**Figure 2** Hybrid MC/MD simulation results showing the crystallographic arrangement of Nb and Zr atoms at 1000 K in **a** 25 and **b** 50 at.%Zr single crystals. Each panel shows Nb and Zr

distribution on one of the {100}, {011} and {111} planes of host bcc lattice. **c** shows a simulation box, where 25 at.%Zr is randomly distributed in the host bcc lattice.

consistent with a recent study on Zr-Nb alloys using phase field simulations [56]. A view of the (011) plane revealed compositional modulations of Nb-rich and Zr-rich near-linear segments, indicating phase separation within the bcc lattices of 25 and 50 at.%Zr single crystals [4, 7, 37]. These modulations were oriented along [100], and their wavelength, representing the distance between two Zr-rich regions, measures approximately 6.8 Å. In this view, the wavelength remained unaffected by the alloy composition, providing a consistent feature across different alloy compositions. However, differences are seen in the Nb-rich and Zr-rich domains on the (111) plane. Such domains possessed irregular shapes, and their sizes varied with Zr content: the Zr-rich domains in 25 at.%Zr were smaller compared to those in 50 at.%Zr. These observations highlight the structural differences and variations domain sizes as a function of Zr composition. Next, we explored the effect of the observed domains on the mechanical response of Nb–xZr (x = 0, 25 and 50 at.%) single crystals.

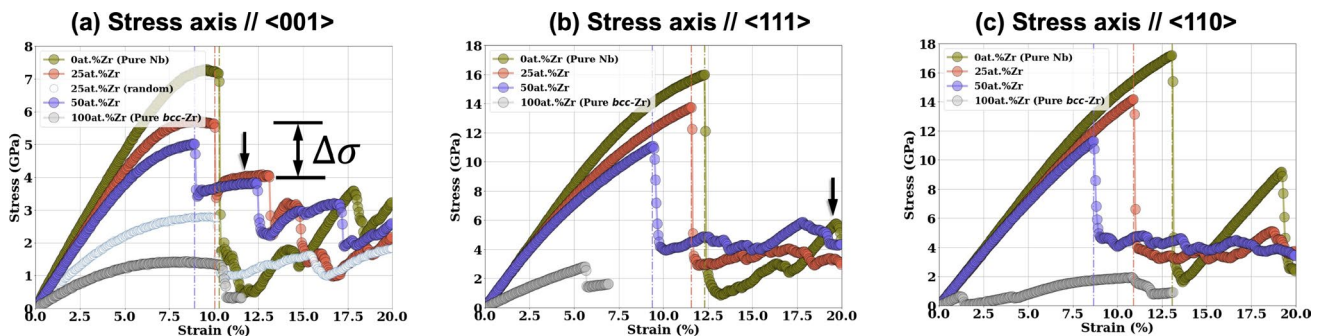
### Mechanical response of single crystals

Figure 3 shows the stress versus strain plots obtained from single crystals under normal tensile stress applied along <100> (Fig. 3a), <110> (Fig. 3b) and <111> (Fig. 3c) crystallographic axes at a temperature of 1000K and a strain rate of 10<sup>8</sup>s<sup>-1</sup>. These plots allow us to compare and contrast the mechanical response of specimens containing 0 at.%Zr (pure Nb), 25 and 50 at.%Zr specimens. Additionally, we have also simulated the mechanical response of bcc Zr (100 at.%Zr) to serve as a control in our analysis.

The results show that the peak strengths ( $\sigma_{\text{peak}}$ ) along <001> direction were nearly half those along <

110> and <111>. The peak strengths followed the trend  $\sigma_{\text{peak}}^{(001)} > \sigma_{\text{peak}}^{(110)} > \sigma_{\text{peak}}^{(111)}$ . Deformation along all three orientations showed a significant drop in strength after reaching peak value, and the corresponding strains marking such drops are shown by dotted lines in Fig. 3a–c. For <110> and <111>-oriented crystals, the abrupt drops in stress occurred immediately after reaching peak stress values (Fig. 3b and c). In contrast, the <001>-orientated crystals exhibited noticeable “deviation from linear elasticity” after reaching the peak value (Fig. 3a), before experiencing a sharp stress drop. Interestingly, this anisotropy in mechanical response up to the point of stress drop remained unaffected by the alloy composition. However, note that for a given orientation, the presence of bcc phase separation did influence the peak strength, the magnitude of stress drop ( $\Delta\sigma$ ) and the subsequent flow stress (region after the dotted lines in Fig. 3a–c).

Figure 3 also shows that the compositional dependence of peak strength, indicating a trend where the peak strengths are in the order of  $\sigma_{\text{peak}}^{0\text{at.\%Zr}} > \sigma_{\text{peak}}^{25\text{at.\%Zr}} > \sigma_{\text{peak}}^{50\text{at.\%Zr}}$ . Furthermore, the pure Nb specimens exhibited the highest  $\sigma_{\text{peak}}$  compared to the specimens containing 25 and 50 at.%Zr. Similarly, the corresponding stress drops followed the order  $\Delta\sigma^{0\text{at.\%Zr}} > \Delta\sigma^{50\text{at.\%Zr}} > \Delta\sigma^{25\text{at.\%Zr}}$ . The ratio  $\frac{\Delta\sigma}{\sigma_{\text{peak}}}$ , which represents the stress drop, varied within ~70–80% for pure Nb (0 at.%Zr), about 40–50% for 25 at.%Zr and around 33–40% for 50 at.%Zr. These findings broadly suggest that an increase in Zr content softens the host bcc lattice. This phenomenon of solute-mediated softening of dilute bcc alloys was observed previously in Re- and W-based alloys, and it was attributed to the positive interaction energy between the dislocation core and solute atom [24, 25]. In the current context, this



**Figure 3** Tensile uniaxial stress–strain plots of single crystals deformed along **a** <001>, **b** <110> and **c** <111> directions. The vertical dotted lines in panels (a)–(c) indicate the onset of plasticity or significant strength loss in the single crystals.

observed softening effect can be explained by the rule of mixtures, where the relative fractions of stiff Nb-rich and softer Zr-rich domains, shown in Fig. 2, determine the overall mechanical response of 25 and 50 at.%Zr via a composite effect. Figure 3 shows that the strength of pure Nb is substantially higher than bcc Zr, indicating that the Zr-rich domains are softer compared to Nb-rich regions. Consequently, the presence of these Zr-rich domains in 25 and 50 at.%Zr specimens reduces their peak strengths compared to pure Nb.

The relative size and distribution of softer Zr-rich domains also play a significant role in determining the relative strengths of 25 and 50 at.%Zr specimens. As shown in the “(111)-view” panels of Fig. 2a and b, the Zr-rich domains in 25 at.%Zr are smaller and more widely distributed spatially compared to those in 50 at.%Zr specimens. By correlating these observations with the stress–strain plots (Fig. 3), we find that the smaller size and higher distribution of Zr-rich domains contribute to the higher peak strength in 25 at.%Zr specimens. This outcome occurs because the softening effect of such domains is spread over a wider area, instead of being localized within specific regions as seen in 50 at.%Zr samples. Conversely, it is worth noting that the “stronger” Nb-rich domains (Fig. 2) also play a role in determining the overall peak strength of 25 and 50 at.%Zr specimens. To investigate this hypothesis, a (001)-orientated single crystal containing a random distribution of Zr atoms with 25 at.%Zr concentration was deformed (see Fig. 2c). The initial structure was energy-minimized and, subsequently, equilibrated at 1000 K, without subjecting it to hybrid MC/MD (see Sect.2). The results showed that  $\sigma_{\text{peak}}$  of this 25 at.%Zr (random) configuration was substantially lower than that of the phase-separated 25 and 50 at.%Zr alloys (Fig. 3a). Hence, the remainder of the manuscript will focus on the deformation behavior of pure Nb (0 at.%Zr) and phase-separated (25 at.% and 50 at.%Zr) specimens). In summary, these results indicate that phase separation within the bcc lattice, and possibly the extent of such separation (compare the (111)-view in Fig. 2), strongly influences the strength and potentially the underlying mechanisms of plasticity in Nb–Zr alloys (see Sects.3.3 and 3.4).

The flow stress curves, representing the stress–strain plots beyond vertical dotted lines in Fig. 3, are reliable indicators of plasticity. A comparison of these curves highlights the impact of bcc phase separation in 25 and 50 at.%Zr, contrasting with response of pure Nb. In

the case of 0 at.%Zr specimens, regardless of orientation, a steady increase in strength was observed after the initial abrupt stress drop, shown by the arrow in Fig. 3b). In contrast, the flow stress response of 25 and 50 at.%Zr specimens substantially differed from that of pure Nb, and the behavior varied depending on the crystal orientation. For phase-separated (001) crystals, a plateau formed around  $\sim 4$  GPa immediately after the initial stress drop (marked with an arrow in Fig. 3a), followed by two smaller stress drops. On the contrary, (110)- and (111)-oriented single crystals exhibited stress values that more or less stabilized within  $\sim 3$ –6 GPa, similar to the behavior observed in ductile face-centered cubic (fcc) single crystals or composite structures containing an FCC phase. Broadly, the examination of flow stress curves of phase-separated 25 and 50 at.%Zr single crystals revealed highly anisotropic plastic deformation at 1000 K and  $10^8 \text{s}^{-1}$ . Therefore, crystal orientation plays a crucial role in determining the underlying deformation mechanisms and the extent to which they influence the overall plasticity. Detailed explanations of those mechanisms are presented in Sects. 3.3 and 3.4.

### Deformation mechanisms in (001)-oriented single crystals

Figure 4 shows MD snapshots illustrating deformation mechanisms in pure Nb (Fig. 4a), 25 at.%Zr (Fig. 4b) and 50 at.%Zr (Fig. 4c) at five “global strain” ( $\epsilon$ ) values. These snapshots show representative mechanisms on the bcc-(1 $\bar{1}$ 0) plane of each specimen. At  $\epsilon = 8.9\%$ , all three materials showed a fine dispersion of fcc phase, indicating a deformation-induced bcc→fcc transformation. This finding is consistent with X-ray and transmission electron microscopy studies of pure Nb, which showed that such a transformation occurs under high strain rate or large deformation conditions [26–29]. As the strain increases to  $\epsilon = 10\%$ , the fraction of fcc qualitatively increased in both pure Nb and 25 at.%Zr specimens. This strain level corresponded to a stress level preceding the abrupt drop in the stress–strain plots of 0 and 25 at.%Zr, as well as the plateau observed on the flow curve of 50 at.%Zr (see Fig. 3a). At  $\epsilon = 10\%$ , deformation in 50 at.%Zr specimen was dominated by twinning, and it contained a visibly smaller fraction of fcc coordinated atoms located at the twin/bcc–matrix interface. Two variants of twins were noted in our simulations: (1 $\bar{1}$ 2)[111] (diagonally oriented) and (112)[11 $\bar{1}$ ]. The horizontal orientation of

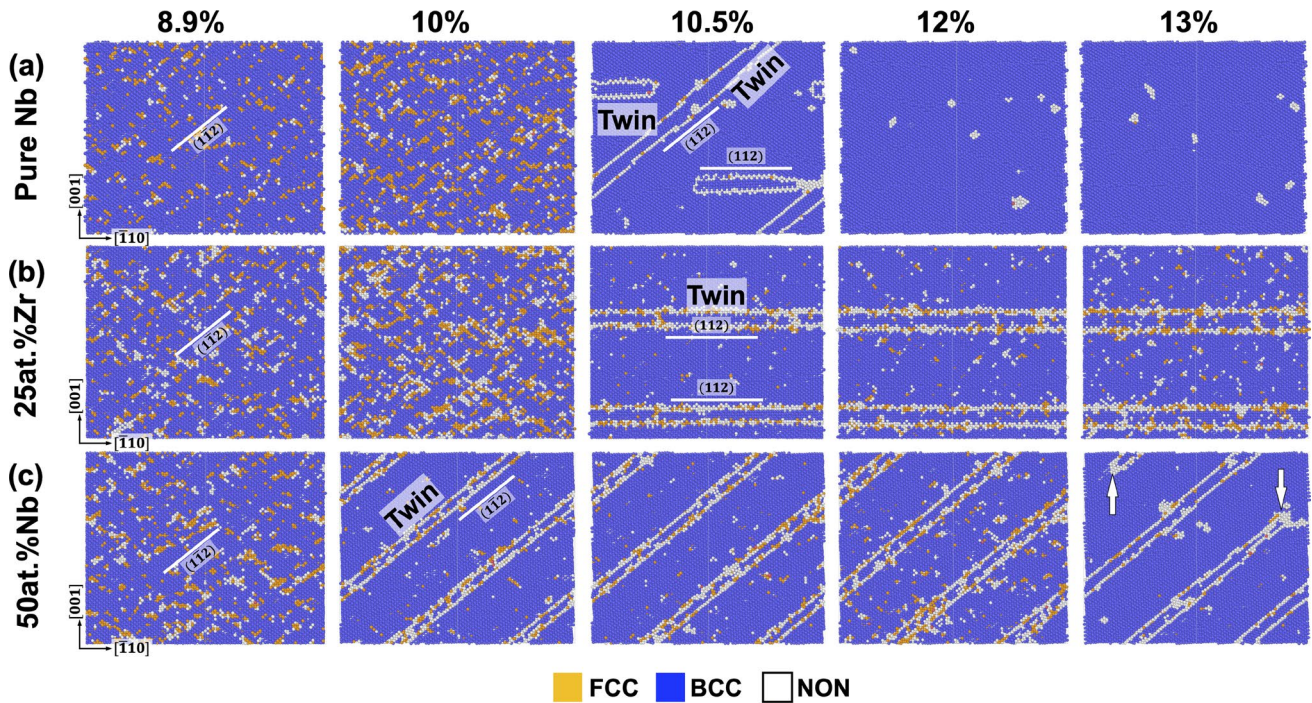


**Figure 4** Simulation results showing deformation features in **a** 25 at.%Zr, **b** 50 at.%Zr and **c** pure Nb single crystals at five strain values. These  $\langle 001 \rangle$ -oriented single crystals were deformed at 1000 K and  $10^8 \text{ s}^{-1}$  strain rate.

$\{112\}[11\bar{1}]$  twins is a visual artifact, because the  $\{110\}$  planes, utilized in the snapshots, cuts through the  $\{112\}$  planes; meaning, lines corresponding to  $\{112\}$  are traces of the actual plane. Notwithstanding, our simulations show twins belonging to the  $\{112\}\langle 111 \rangle$  family, similar to those seen in pure Nb [17, 28, 29].

After a strain ( $\epsilon$ ) of 10.5%, all three compositions exhibited  $\{112\}\langle 111 \rangle$  twinning as their dominant deformation. This mode persisted in 25 and 50 at.%Zr specimens until  $\epsilon = 13\%$ . However, for pure Nb, deformation twinning was not observed beyond  $\epsilon = 12\%$  as the deformation was dominated by dislocation plasticity (see Fig. 5a). In contrast, Fig. 5b shows that within the strain range  $\epsilon = 10.5\text{--}13\%$ , the 25 at.%Zr specimen did not contain any dislocations and its deformation was driven by twinning. In 50 at.%Zr specimens, the dislocation substructure coexisted with twins at  $\epsilon = 13\%$ . A comparison of corresponding panels in Figs. 4c and 5c indicate that twins were receding (marked by arrows) in structure deformed at  $\epsilon = 13\%$ . These results show that twins are replaced by dislocation substructure as the materials are strained to higher values. Importantly, a comparison of deformation features at  $\epsilon = 10.5, 12$  and  $13\%$  (Fig. 4) highlights that phase

separation of bcc into Nb-rich and Zr-rich domains (Fig. 2) facilitated twinning at 1000 K.

Comparing the stress–strain plots presented Fig. 3a, we note that the bcc  $\rightarrow$  fcc transformation had occurred prior to the abrupt stress drop (indicated by dotted lines in Fig. 3a). In the following, we will refer to this portion of the stress–strain plots as “elastic–inelastic” deformation regime, which describes the elastic deformation of the host bcc lattice, and its transformation into the fcc phase. Portion of plots immediately following the abrupt stress drop will be referred to as the “plastic” region as the flow stress was largely influenced by the formation of twins and dislocations (see Figs. 4 and 5).

The results presented in Fig. 4 have provided two mechanism-based insights into the stress–strain response of  $\langle 001 \rangle$ -oriented single crystals (see Fig. 3a). Firstly, a plateau is observed in the plastic regime of 25 and 50 at.%Zr specimens. This was attributed to the formation and persistence of  $\{112\}\langle 111 \rangle$  twins. Additionally, a secondary abrupt change is also observed toward the end of that plateau. By correlating the data presented in Fig. 3a and Fig. 4, it is evident that the drop was a consequence of nucleation and multiplication of dislocations that gradually replace twins. Secondly, the initiation of elastic–inelastic and plastic

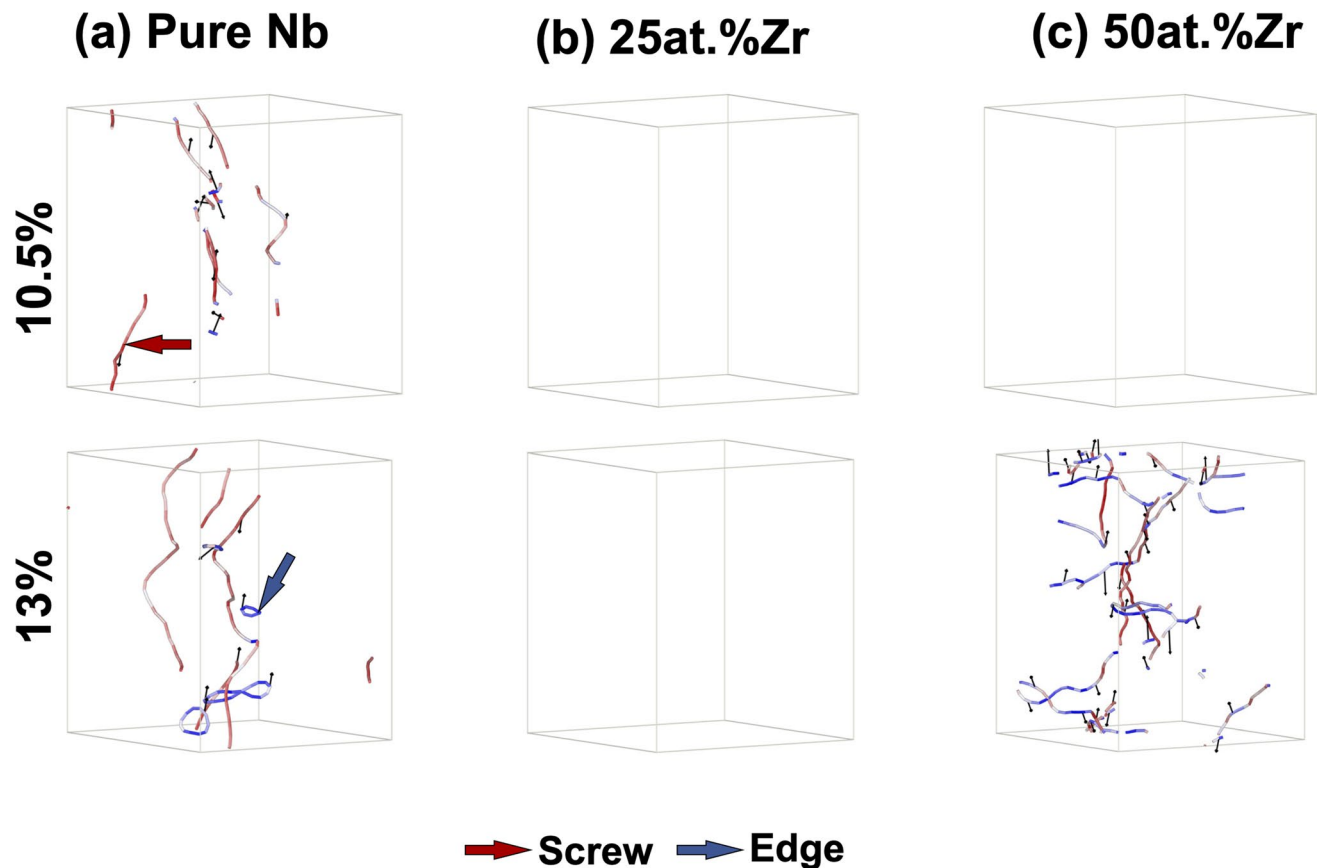


**Figure 5** Dislocation substructures observed in **a** pure Nb, **b** 25 at.%Zr and **c** 50 at.%Zr  $\langle 001 \rangle$ -oriented single crystals at 10.5 and 13% tensile strain values after deforming them along  $\langle 001 \rangle$  at 1000 K.

deformation is linked to the bcc  $\rightarrow$  fcc transformation, where the fcc phase appears to facilitate twinning via coexistence in both 25 and 50 at.%Zr specimens. However, the qualitative results presented in Fig. 4 do not sufficiently explain the effect of composition on deformation-induced fcc transformation. To address this aspect, a comparison has been made among the three compositions, by studying the variation in fcc volume fraction with strain.

Figure 6a compares the fcc fraction v.s. strain plots for 0, 25 and 50 at.%Zr specimens. These plots can be subdivided into two regimes: The first regime corresponds to the elastic–inelastic portion of the stress–strain response while the second regime represents the plastic portion (see Fig. 3a). In the elastic–inelastic portion, both pure Nb (0 at.%Zr) and 25 at.%Zr show a monotonic increase in fcc fraction to a maximum value of  $\sim 21\%$ , while 50 at.%Zr was limited to  $\sim 13\%$  fcc fraction. The significant fcc fractions in these compositions may explain the deviation from linear elasticity, as seen from the curvature in their

stress–strain plots around the peak stress (see Fig. 3a). Within the plastic regime, both 25 and 50 at.%Zr monotonically reached a peak fcc fraction value of 10%, while the pure Nb contains a negligible fcc fraction. This indicates that phase separation within the bcc lattice of 25 and 50 at.%Zr may predispose them toward fcc formation and fcc-mediated twinning (as seen in panels for  $\epsilon = 10$ –13% in Fig. 4). The inset in the top right-hand corner of Fig. 6a shows the early stages of fcc formation for each composition. We find that onset strains for fcc formation follow the trend: 0 at.%Zr  $>$  25 at.%Zr  $>$  50 at.%Zr, indicating that the phase-separated 25 and 50 at.%Zr alloys undergo fcc transformation earlier than pure Nb. This early onset of bcc  $\rightarrow$  fcc transformation introduces inelastic deformation within the  $\langle 001 \rangle$ -oriented single crystals, which may lower the peak stress/strength compared to  $\langle 001 \rangle$ -oriented pure Nb (as shown in Fig. 3a).

To understand the inelastic deformation mechanism in  $\langle 001 \rangle$ -oriented single crystals, we studied the local strain distribution and crystallography using 25

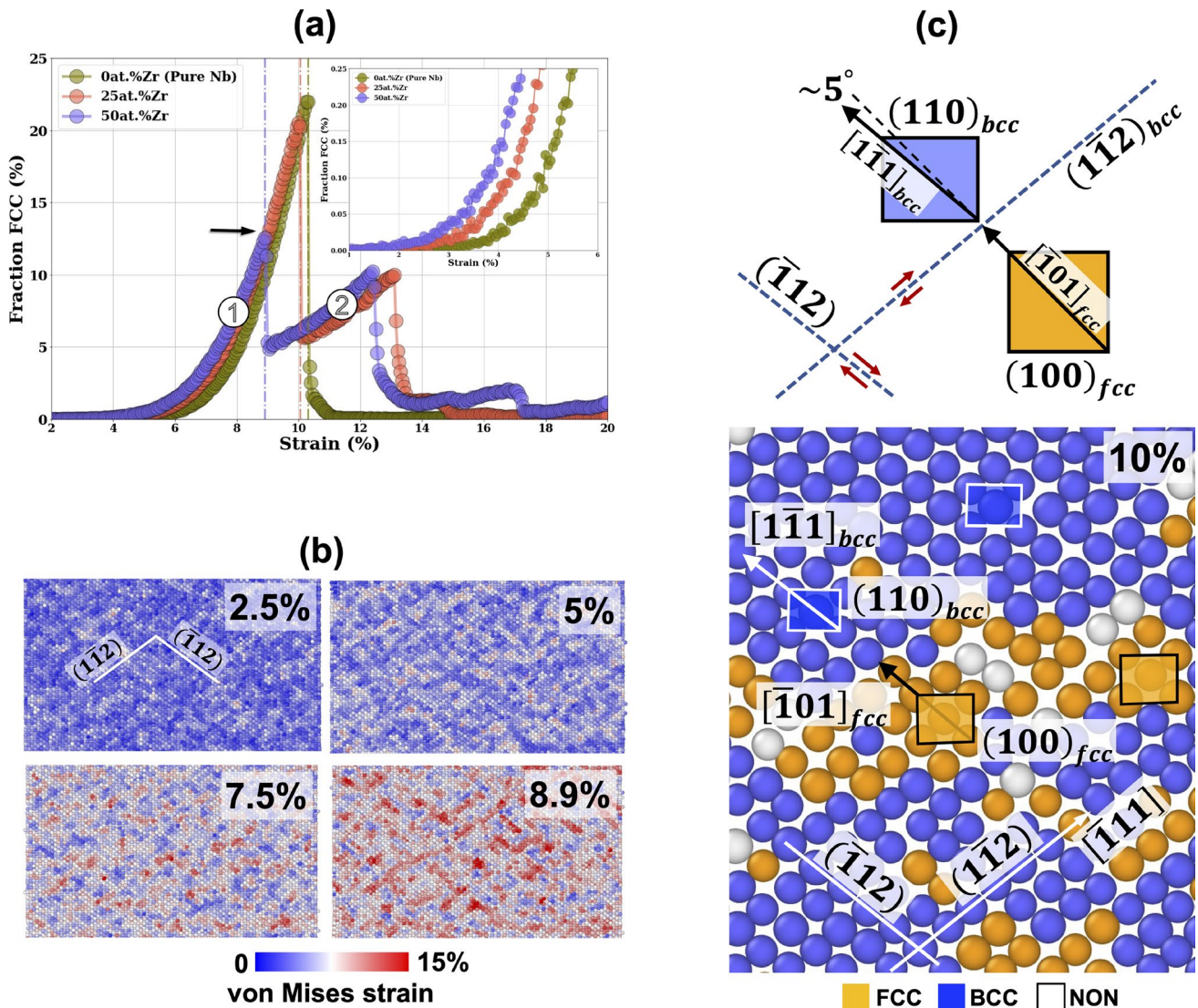


**Figure 6** a Plots showing the deformation-induced fcc fraction v.s. tensile strain single crystals that were deformed along  $\langle 001 \rangle$ . Inset in panel “a” shows the early stage of fcc formation. b (110)

plane views showing von Mises strain distribution in 25 at.%Zr. c shows the bcc/fcc crystallographic orientation relationship at 10% strain.

at.%Zr as a representative system. Figure 6b shows the distribution of von Mises shear strain on a bcc-(110) plane at four global strain values ( $\epsilon = 2.5, 5.0, 7.5$  and  $8.9\%$ ). These strains were localized along two conjugate planes of  $(\bar{1}\bar{1}2)$  and  $(1\bar{1}2)$ , with their magnitudes increasing with larger  $\epsilon$  values. These results indicate that overall deformation along  $\langle 001 \rangle$  induces in-plane shear between the bcc- $\{112\}$  planes, thereby promoting bcc  $\rightarrow$  fcc transformation via a displacive mechanism [4]. Figure 6c shows the crystallographic change caused by this mechanism. The in-plane shear on the two conjugate planes,  $(\bar{1}\bar{1}2)$  and  $(1\bar{1}2)$ , caused

the deformation of the bcc-(110) plane (marked by blue-colored rectangular motifs) into (100) planes of fcc (marked by orange-colored square motifs). Notably, the fcc- $[\bar{1}01]$  direction was slightly misaligned by approximately  $5^\circ$  with respect to bcc- $[\bar{1}\bar{1}1]$ . This crystallographic arrangement gave rise to the *Pitsch* orientation relationship:  $(110)_{bcc} // (110)_{fcc}$  and  $[\bar{1}\bar{1}1]_{bcc} // [\bar{1}01]_{fcc}$  (see Fig. 6c). Furthermore, within the plastic regime, an increase in  $\epsilon$  resulted in the in-plane bcc- $\{112\}$  shear transforming fcc domains into  $\{112\}\langle 111 \rangle$  twins. This phenomenon is exemplified in Fig. 4, which shows the presence of fcc coordinated atoms

inside twins and at the twin/matrix interfaces. Currently, studies are ongoing to understand the energetics of fcc→bcc-twin formation in phase-separated 25 and 50 at.%Zr alloys. In the following sections, we present the observed deformation mechanisms in  $\langle 110 \rangle$ - and  $\langle 111 \rangle$ -oriented single crystals.

### Deformation mechanisms in $\langle 111 \rangle$ - and $\langle 110 \rangle$ -oriented single crystals

In contrast to  $\langle 001 \rangle$ -oriented crystals, deformation along  $\langle 111 \rangle$  and  $\langle 110 \rangle$  directions resulted in minimal fcc formation within the inelastic and plastic regimes. The volume fractions of fcc regions were significantly lower by approximately two orders of magnitude than in  $\langle 001 \rangle$  oriented crystals (see Appendix 1). Notably,  $\{112\}\langle 111 \rangle$  twinning was not observed after straining along  $\langle 111 \rangle$  and  $\langle 110 \rangle$ . Instead, plastic deformation in these crystals was dominated by the nucleation and multiplication of dislocations.

The initiation of plastic deformation in these crystals was due to the nucleation of dislocation loops, and their formation correlated with the stress drop observed in the stress–strain plots (Fig. 3). Figure 7a and b shows examples of dislocation loops in pure Nb

and 25 at.%Zr, respectively, when viewed along  $\langle 111 \rangle$  family of directions. These loops were characterized by a  $\frac{1}{2}\langle 111 \rangle$  Burgers vector and were tilted out of the densely packed  $\{110\}$  planes of bcc. In the specific cases shown in Fig. 7, the normal to the dislocation loop plane (demarcated by solid black lines) was tilted by approximately  $7\text{--}8^\circ$  with respect to the  $\{110\}$  plane normal (shown by black dotted lines). We monitored the multiplication tendencies of such precursory  $\frac{1}{2}\langle 111 \rangle$  dislocations by measuring their densities as a function of the imposed strain.

In Fig. 8, panels (a1) and (b1) show the measured dislocation densities in the  $\langle 110 \rangle$ - and  $\langle 111 \rangle$ -oriented crystals, respectively. The corresponding percentage drop from the maximum dislocation density for each alloy composition is shown in panels 8(a2) and 8(b2). Anisotropy in dislocation densities is mainly seen during the plastic deformation of 25 at.%Zr, while pure Nb and 50 at.%Zr showed comparable responses (compare Fig. 8a1 and 8b1). At the onset of plasticity, pure Nb contained the highest dislocation density, while 50 at.%Zr had the lowest (Fig. 8a1 and 8b1). Subsequently, dislocation density in pure Nb rapidly reduces by  $\sim 90\%$  compared to other two materials. In contrast, dislocation density in 25 and 50 at.%Zr

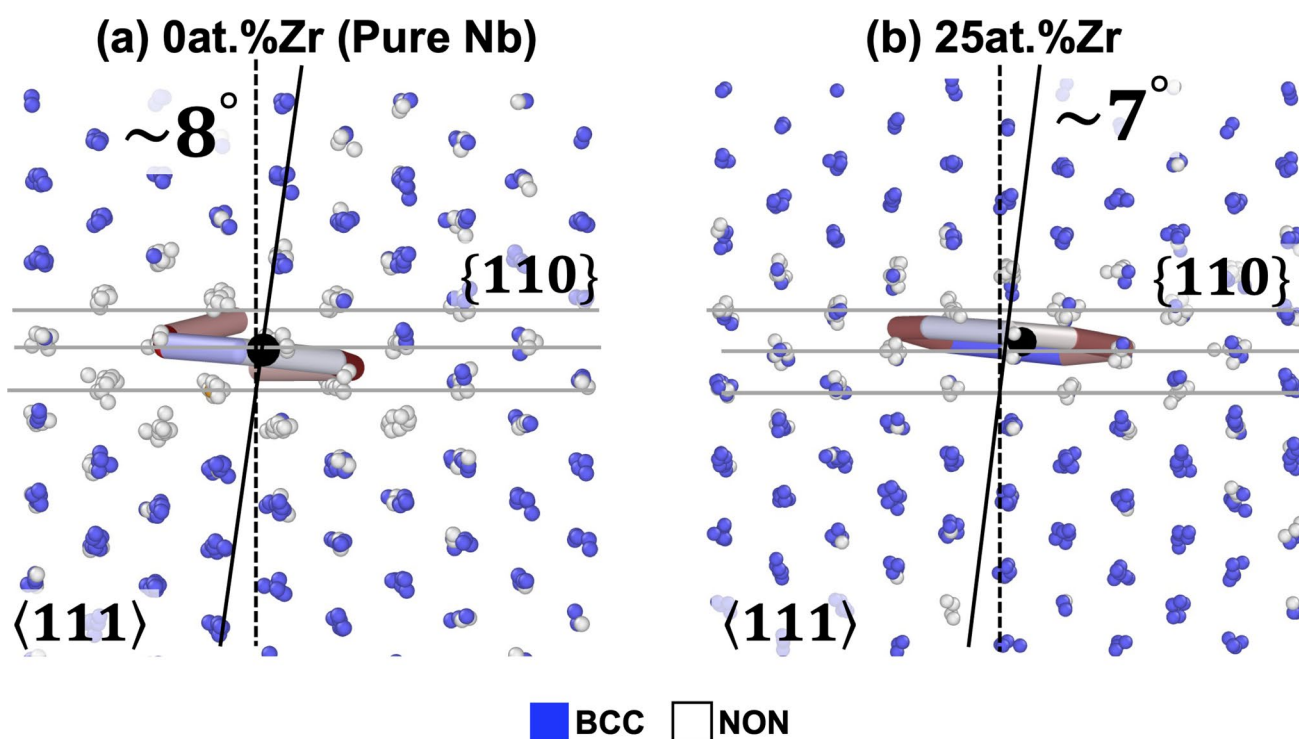


**Figure 7** Simulation snapshots showing dislocation loops that initiated plasticity in **a** pure Nb and **b** 25 at.%Zr single crystals deformed along  $\langle 011 \rangle$ . The loop edges are viewed along a  $\langle 111 \rangle$ , and the horizontal lines represent planes in the  $\{011\}$  family.

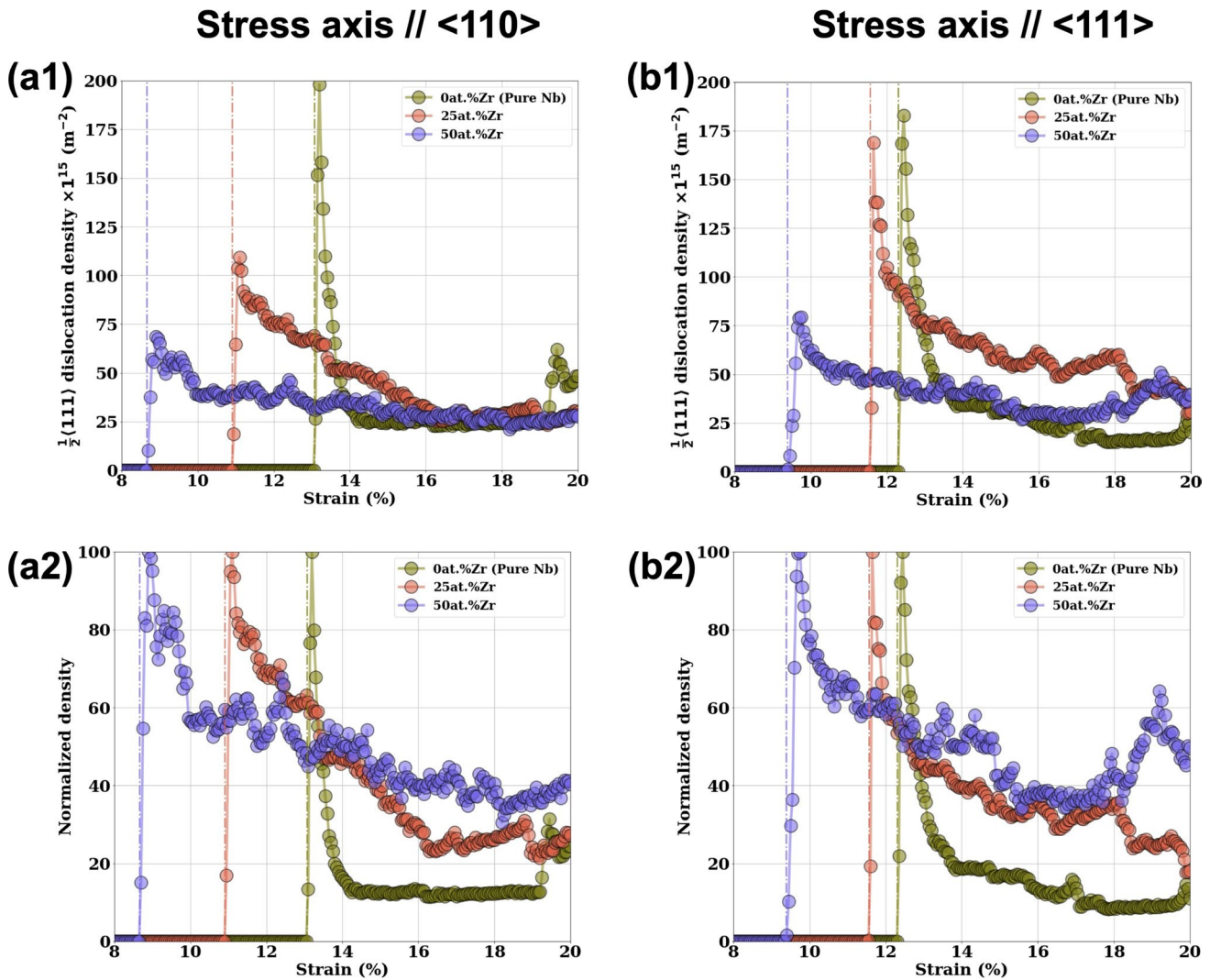


**Figure 8** Plots showing the variation in dislocation density with strain in single crystals deformed along (a1)–(a2)  $\langle 110 \rangle$  and (b1)–(b2)  $\langle 111 \rangle$ . Panels (a1) and (b1) show the actual densities, while (a2) and (b2) show the normalized densities in percentage.

decreased gradually to around 60–75% in both crystals, unlike pure Nb (Fig. 8a2 and 8b2). Broadly, the observed trends in dislocation density versus strain plots in Fig. 8a1 and 8b1 can be explained in terms of the competition between dislocation formation and thermally assisted dislocation–dislocation annihilation [57, 58].

Plastic deformation is initiated through the rapid multiplication of precursory dislocation loops, as shown in Fig. 7. This tendency appears to be more pronounced in pure Nb compared 25 and 50 at.%Nb. However, at a high temperature of 1000 K, the mobile  $\frac{1}{2}\langle 111 \rangle$  dislocations start to annihilate each other. In the absence of grain boundaries, this annihilation mechanism likely results from the attraction of

dislocations with opposite senses and/or Burgers vectors [17]. A comparison of Fig. 8a2 and 8b2 suggests that such annihilation tendency is more prevalent in pure Nb than 25 and 50 at.%Zr. To study this issue, we have compared this dislocation–dislocation annihilation tendency in pure Nb, 25 and 50 at.%Zr by using the screw dislocation quadrupole geometry shown in Fig. 1c. These simulations involved performing hybrid MC/MD up to 5 million iterations at 1000 K (see Sect. 2). The simulation results, shown in Fig. 9, reveal that 25 and 50 at.%Zr retain the prior screw dislocations (discussed later), while they are completely annihilated at in pure Nb. Crucially, these results demonstrate that phase separation within Nb–Zr significantly affects dislocation configurations.

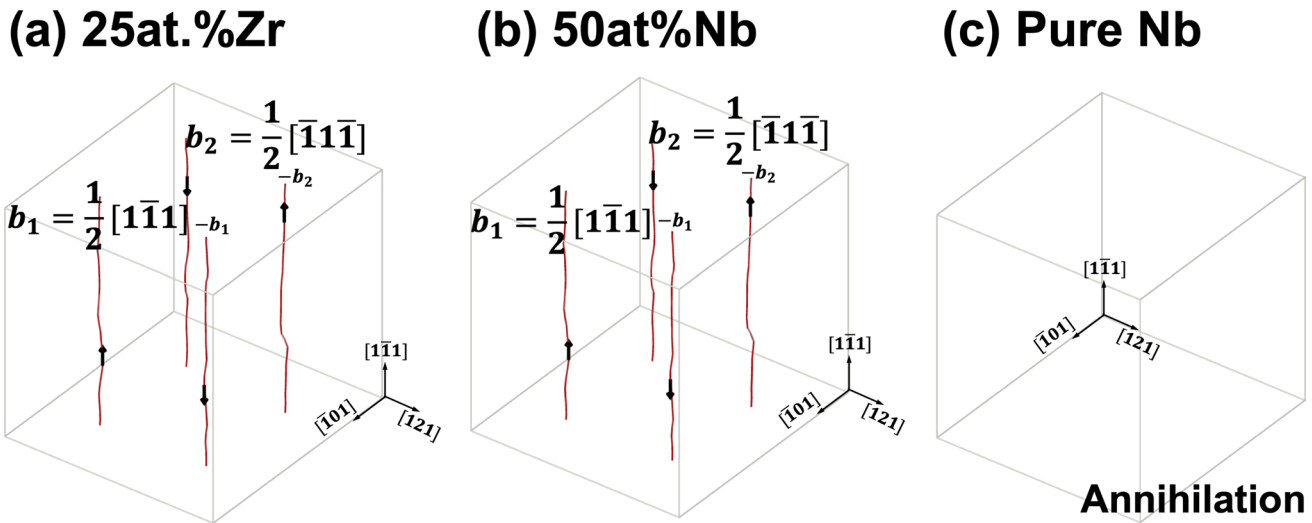


**Figure 9** Hybrid semi-grand canonical Monte Carlo and molecular dynamics simulation results—after 5 million iterations—compare dislocation quadrupole configurations in **a** 25 at.%Zr,

**b** 50 at.%Zr and **c** pure Nb single crystals at 1000 K. External stress was not applied to these single crystals.

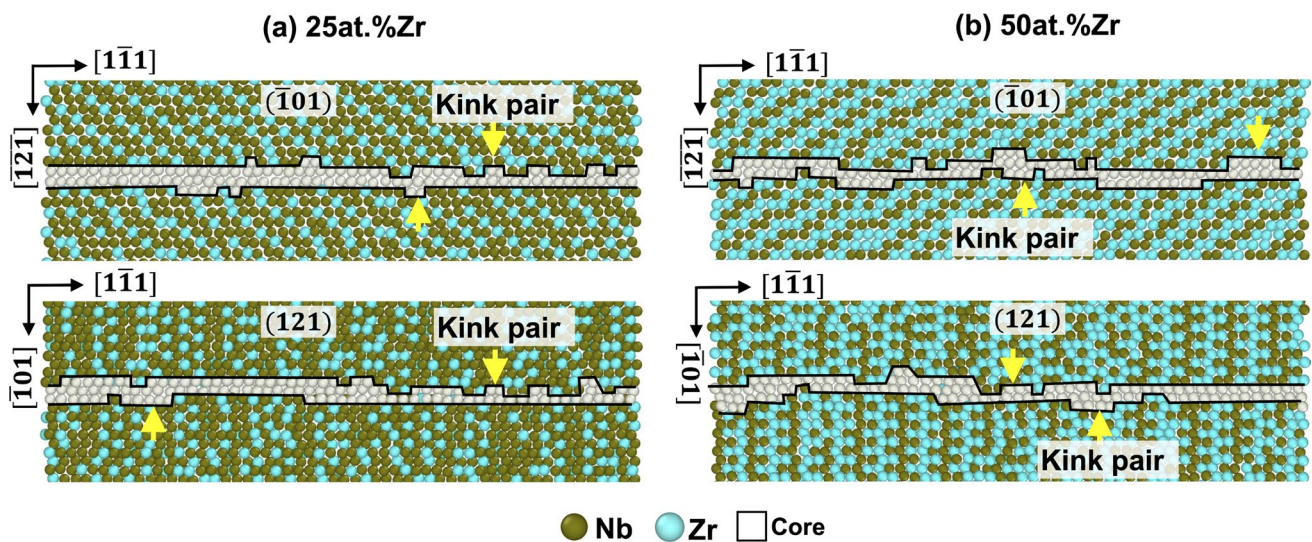


**Figure 10** Simulation results showing the spreading of  $\frac{1}{2}\langle 111 \rangle$  screw dislocation core on  $(\bar{1}01)$  and  $(121)$  planes in **a** 25 at.%Zr and **b** 50 at.%Zr. The “core” atoms were identified using the

PTM and DXA algorithms. These were atoms that could not be associated with either bcc or fcc coordination, and were proximal to the dislocation lines.

Finally, we have qualitatively examined the core structures in 25 and 50 at.%Zr by extracting them from their respective quadrupoles (Fig. 9). Figure 10 shows two representative views of the screw dislocation cores lying on  $(\bar{1}01)$  and  $(121)$  planes of 25 at.%Zr (Fig. 10a) and 50 at.%Zr (Fig. 10b). It is well known that the cores of screw dislocations in bcc crystals tend to spread themselves on other planes rather than

being confined to the densely packed  $\{110\}$  planes [17]. Our simulations qualitatively capture this aspect and show the spread of screw dislocation cores in 25 and 50 at.%Zr over  $(\bar{1}01)$  and  $(121)$ . In Fig. 10, the spatial extent of the cores is marked by bold black lines. We also find that the contour of the cores consists of several closely spaced *kink pairs* along the dislocation line, as indicated with arrows. The lateral spreading of kink

pairs in opposite directions moves the dislocations forward, and that occurs via thermal activation and/or under the influence of stress [17]. In general, the lateral movement of kinks face hindrance by two factors common to all three materials, including pure Nb. Firstly, the close proximity of kink pairs can generate repulsive forces that counteract their lateral motion. Secondly, the necessity for lateral movement across multiple planes, such as  $(\bar{1}01)$  and  $(121)$ , adds complexity to their mobility. It is worth noting that these factors do not explicitly consider the influence of composition. Nevertheless, interactions of kink pairs with the compositional modulation, resulting from phase separation within the bcc lattice of alloys containing 25 at.% and 50 at.% Zr, are likely to impede their movement. Consequently, the thermally activated dislocation movement in these two alloys might be slow and steady even under stresses at 1000 K, which delays the tendency for approaching dislocations to annihilate (compared to pure Nb). This aspect of dislocation motion is currently under investigation and is the subject of a separate study.

## Discussion

Our simulations showed that annealing Nb-based alloys at 1000 K causes phase separation of the underlying bcc lattice into Nb-rich (Zr-lean) and Zr-rich (Nb-lean) domains. Two key insights are evident from the mechanical response of such *phase-separated* Nb-Zr single crystals, under high temperature (1000 K) and strain rate ( $10^8 \text{ s}^{-1}$ ). First, the presence of Zr-rich domains softened the bcc lattice by reducing the stress required to initiate plastic deformation compared to pure Nb. The relatively “harder” Nb-rich domains strengthened the Nb-Zr alloys compared to a random Nb-Zr solid solution. We note that solute-induced softening of bcc alloys has been previously reported [24, 25]. Our results show that such softening can also occur due to relatively higher length scale structural alterations such as the phase separation phenomenon shown here. Second, deformation mechanism in the elastic (and inelastic) and plastic regimes is highly anisotropic, and such orientation-dependent deformation is best understood by the following mechanism:

- (i) Deformation along  $\langle 110 \rangle$  and  $\langle 111 \rangle$  directions shifts from elastic behavior to dislocation plasticity
- (ii) Deformation along  $\langle 001 \rangle$  directions is initially elastic with fcc formation (inelastic response). It subsequently transitions to  $\{112\}\langle 111 \rangle$  twinning and further fcc formation, and ultimately leading to dislocation plasticity

The bcc→fcc transformation pathway is particularly useful to understand our results. Past experimental studies on pure Nb have reported this deformation-induced transformation [2, 26–29]. Our MD simulations have also captured this bcc→fcc transition in pure Nb, which is consistent with extant experimental reports and validates the transferability of the semiempirical potential employed in this work. Importantly, these simulations demonstrate that the deformation-induced bcc→fcc transformation is dependent on the crystallographic orientation, and is influenced by the concentration of Zr. For example, the inset in Fig. 6a indicates that the presence of Zr reduces the onset strain for this transformation. This implies that the transformation kinetics differ between pure Nb and Nb alloys with 25 and 50 at.%Nb. We quantified the kinetics using the well-known Johnson–Mehl–Avrami–Kolmogorov (JMAK) equation [59, 60]:

$$X_{\text{fcc}}(t) = 1 - \exp[Kt^n], \quad (1)$$

where  $X_{\text{fcc}}$  is the fcc volume fraction,  $t$  is time,  $K$  is the rate constant measuring the speed of transformation and the Avrami exponent  $n$  signifies the dimensionality of transformation ( $n \geq 3$  and  $n \geq 2$  indicate a three-dimensional volumetric transformation and two-dimensional features, respectively) [59, 60]. Taking natural logarithm of Eq. 1 twice yields a linear equation  $\text{Ln}(-\text{Ln}[1 - X_{\text{fcc}}(t)]) = -\text{Ln}(K) + n \times \text{Ln}(t)$ , whose slope and intercept quantify  $n$  and  $K$ , respectively.

Figure 11a and b shows  $\text{Ln}(-\text{Ln}[1 - X_{\text{fcc}}(t)])$  versus  $\text{Ln}(t)$  plots of data extracted from the elastic–inelastic and plastic regimes in Fig. 6a, respectively. Those regimes are also indicated in the insets of Fig. 6a and b. Figure 11a qualitatively demonstrates the effect of Zr concentration in the inelastic regime, because the slope ( $n$ ) and intercepts ( $-\text{Ln}(K)$ ) depend on the Zr content. In contrast, the slope of the plastic regime appears to be unaffected by the Zr concentration (Fig. 6b).

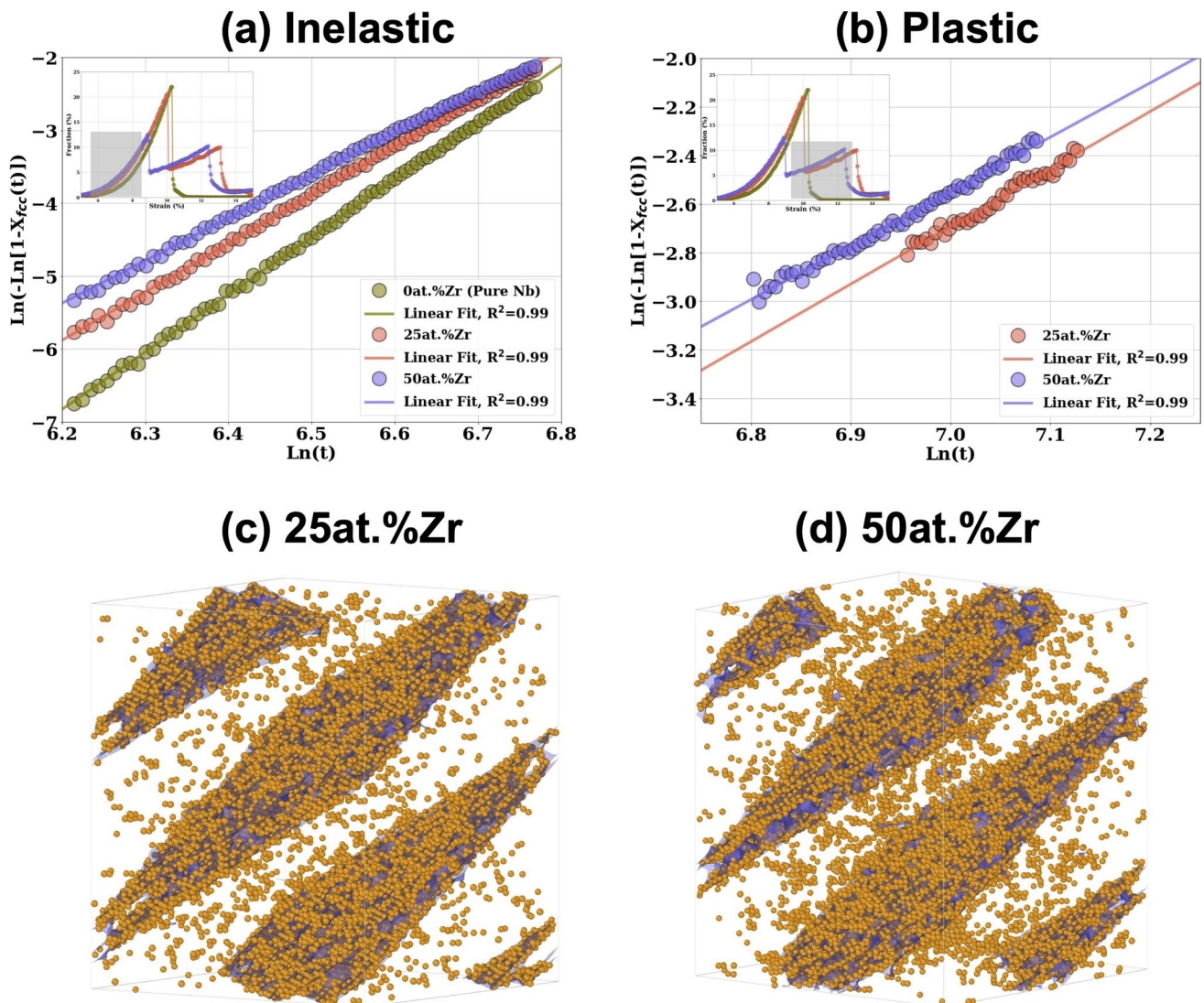


**Figure 11** Johnson–Mehl–Avrami–Kolmogorov plots of compositions manifesting fcc phase during **a** inelastic and **b** plastic deformation regimes. Insets show that the fcc vol. fraction v.s. strain plots, where the shaded areas indicate different regimes of deformation. **c** and **d** show that fcc coordinated atoms are

predominantly located at the bcc/twin boundaries in 25 and 50 at.%Zr, respectively. These twins formed after 10.% tensile strain along  $\langle 001 \rangle$ . Interfaces in **c** and **d** are denoted using transparent blue-colored contours.

**Table 1** List of computed Johnson–Mehl–Avrami–Kolmogorov parameters as a function of Zr concentration

Nominal concentration (at.%Zr)*	Inelastic ( $n, K$ )	Plastic ( $n, K$ )
0 or pure Nb	7.9, $6.8 \times 10^{-25}$	–
25 (27.5)	6.6, $3.8 \times 10^{-21}$	2.3, $4.3 \times 10^{-9}$
50 (51.4)	5.8, $9.0 \times 10^{-19}$	2.2, $1.3 \times 10^{-8}$

\* Actual Zr concentrations are in parentheses

Table 1 lists  $n$  and  $K$  values that were extracted from the plots presented in Fig. 11a and b. In the inelastic regime, the rate constant  $K$  follows the trend  $K^{50 \text{ at.\%Zr}} > K^{25 \text{ at.\%Zr}} > K^{\text{pure Nb}}$ , and within the plastic regime,  $K^{50 \text{ at.\%Zr}} > K^{25 \text{ at.\%Zr}}$ . These trends show that the rate of bcc  $\rightarrow$  fcc transformation is influenced by Zr concentration, causing earlier fcc formation during straining compared to pure Nb (see inset in Fig. 6a). In the inelastic regime, the Avrami exponents were consistently exceeded 3, and their order was  $n^{50 \text{ at.\%Zr}} < n^{25 \text{ at.\%Zr}} < n^{\text{pure Nb}}$ .

The values  $n \geq 3$  suggest that the bcc→fcc transformation occurs volumetrically. This observation is consistent with Fig. 6b, which shows that fcc formation is closely associated with the shearing of bcc lattice planes. The compositional dependence of the exponent  $n$  in the inelastic regime is likely because of higher-order effects such as coupling between compositional modulations (Fig. 2) and shear strain distribution within the bcc lattice (Fig. 6b) [4].

In the plastic regime, Avrami exponents of 25 at.%Zr ( $n = 2.3$ ) and 50 at.%Zr ( $n = 2.2$ ) was comparable to  $\sim 2$ , which implies that fcc formation is likely associated with two-dimensional (2D) features [59, 60]. The examination of bcc–matrix/twin boundaries, presented in Fig. 11c and d, showed that fcc coordinated atoms indeed lie predominantly on 2D interfaces. Taken together, MD simulations of deformed  $\langle 001 \rangle$ -oriented single crystals and the corresponding JMAK analysis of bcc→fcc transformation in the plastic regime revealed that fcc formation is associated with  $\{112\}\langle 111 \rangle$  twinning in bcc Nb–Zr alloys.

Finally, our findings have implications on the mechanical reliability of alloys that are located in the Nb-rich corner of the Nb–Zr phase diagram. In particular, conditions that induce high local stress facilitate the nucleation and propagation of the crack front [29, 61]. This failure mechanism is pervasive and manifests in materials regardless of the applied strain or loading rates [61, 62]. This suggests that stress-induced bcc→fcc transformation in  $\sim 25$ –50 at.%Zr alloys can help in delaying catastrophic failure by blunting the progression of crack tips. This beneficial influence of prior bcc lattice phase separation is particularly relevant in coarse-grained materials. However, its impact on fine-grained materials, where grain boundaries play a significant role in mechanical strength, remains to be examined.

## Summary

In this study, we investigated the effect of phase separation on the mechanical response of body-centered cubic (bcc) Nb–Zr alloys under extreme conditions. We performed hybrid Monte Carlo (MC)/Molecular Dynamics (MD) simulations at 1000 K to induce phase separation in Nb-25 at.%Zr and Nb-50 at.%Zr

single crystals, and compared them with a pure (bcc) Nb reference crystal. These specimens were subjected to deformation at 1000 K and  $10^8 \text{ s}^{-1}$  strain rate using MD simulations. We deformed the single crystals along  $\langle 001 \rangle$ ,  $\langle 110 \rangle$  and  $\langle 111 \rangle$  directions to probe the directional dependence of the mechanical response of Nb– $x$ Zr ( $x = 0, 25$  and 50 at.%) alloys. Results and implication of this study are summarized below:

- (1) Nb-25 at.%Zr and Nb-50 at.%Zr exhibited phase separation into iso-structural, bcc Zr-rich and Nb-rich domains at 1000 K. Notably, the Zr-rich domains in Nb-25 at.%Zr were finer compared to those in Nb-50 at.%Zr.
- (2) The mechanical testing showed a reduction in peak stresses with increasing Zr concentration: pure Nb > 25 at.%Zr > 50 at.%Zr. Such composition-dependent strength reduction was attributed to the presence of “softer,” bcc Zr-rich domains in the phase-separated bcc lattice. In 50 at.%Zr, the coarser Zr-rich domains further contributed to the reduction in strength.
- (3) Deformation pathways showed high anisotropy when Nb– $x$ Zr single crystals were strained along  $\langle 001 \rangle$ ,  $\langle 110 \rangle$  and  $\langle 111 \rangle$  directions. The deformation mechanisms can be summarized as follows
  - (a)  $\langle 110 \rangle$  and  $\langle 111 \rangle$ : Elastic → dislocation plasticity
  - (b)  $\langle 001 \rangle$ : Elastic + volumetric fcc formation →  $\{112\}\langle 111 \rangle$  twinning + interfacial fcc formation → dislocation plasticity
- (4) In the  $\langle 001 \rangle$ -oriented crystals, a bcc→fcc transformation was observed leading to  $\{112\}\langle 111 \rangle$  twinning within the bcc lattice of Nb– $x$ Zr. This stress-induced phase transition resulted in the formation of fcc structures both within the bulk of bcc lattice (volume dominated) and at the twin/bcc interface (interface dominated).
- (5) Our results collectively show that the softening of bcc alloys can be correlated to a combination of factors such as crystalline anisotropy, local solute segregation, bcc→fcc displacive phase transformation and twinning. Thus, our work compliments current understanding of softening in bcc metals, which was largely associated with dislocation movement alone.

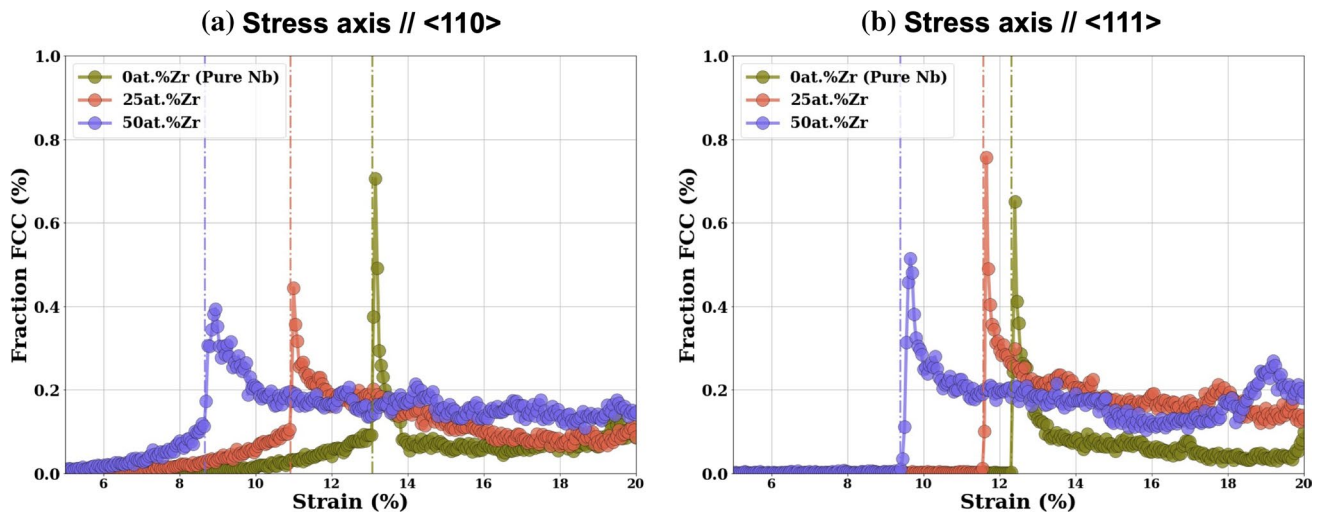


**Figure 12** Plots showing the compositional dependence of fcc fraction v.s. strain in **a**  $\langle 110 \rangle$ - and **b**  $\langle 111 \rangle$ -oriented single crystals. The vertical dotted lines correspond strains where abrupt drop in strength were noted in their stress strain plots.

## Acknowledgements

MH and DC is grateful for partial funding from the Army Research Laboratory under the Cooperative Agreement No. W911NF-20-2-0190. DC also acknowledges computation time on the Pittsburgh Supercomputing Center's Bridges-2 cluster that was allocated through NSF-XSEDE MAT200006 and the Alpine High Performance Computing resource at the University of Colorado Boulder. Alpine is jointly funded by the University of Colorado Boulder, the University of Colorado Anschutz, Colorado State University and the National Science Foundation (award 2201538). SGS acknowledges support from the US Air Force Office of Scientific Research grant FA9550-20-1-0169.

## Author contributions

MH was involved in data curation (equal), formal analysis (equal), investigation (equal), methodology (equal), software (equal) and writing—original draft (equal). SGS was responsible for conceptualization (equal), methodology (equal), funding acquisition (equal) and writing—reviewing and editing (equal). DC contributed to conceptualization (equal), funding acquisition (equal), methodology (equal), project administration (equal), resources (equal), supervision (equal), visualization (equal) and writing—reviewing and editing (equal).

## Funding

Open access funding provided by SCEL, Statewide California Electronic Library Consortium.

## Data and code availability

Data can be made available upon reasonable request.

## Declarations

**Conflicts of interest** The authors declare that they have no known competing financial interests or personal relationships that could have appeared to influence the work reported in this paper.

**Ethical approval** Not applicable.

**Open Access** This article is licensed under a Creative Commons Attribution 4.0 International License, which permits use, sharing, adaptation, distribution and reproduction in any medium or format, as long as you give appropriate credit to the original author(s) and the source, provide a link to the Creative Commons licence, and indicate if changes were made. The images or other third party material in this article are included in the article's Creative Commons licence,

unless indicated otherwise in a credit line to the material. If material is not included in the article's Creative Commons licence and your intended use is not permitted by statutory regulation or exceeds the permitted use, you will need to obtain permission directly from the copyright holder. To view a copy of this licence, visit <http://creativecommons.org/licenses/by/4.0/>.

### Appendix 1: bcc→fcc transformation during the deformation of $\langle 110 \rangle$ - and $\langle 111 \rangle$ -oriented single crystals

Plots presented in Fig. 12 compares the fcc formation in deformed  $\langle 110 \rangle$  (Fig. 12a) and  $\langle 111 \rangle$  (Fig. 12b) single crystals. Comparison with Fig. 12a showed that fcc fraction in these crystals were substantially lower compared to the  $\langle 001 \rangle$ : Maximum fcc fraction in  $\langle 110 \rangle$ - and  $\langle 111 \rangle$ -oriented single crystals was *two orders of magnitude lower* than  $\langle 001 \rangle$ . This comparison also demonstrates that deformation-induced bcc→fcc transformation is highly anisotropic. Still, the plots presented in Fig. 12 share a key commonality with those deformed along  $\langle 001 \rangle$ . Higher Zr content appears facilitates early onset of fcc formation compared to pure Nb.

### References

- [1] Tan Y, Ma C, Kasama A, Tanaka R, Mishima Y, Hanada S, Yang J-M (2003) Effect of alloy composition on microstructure and high temperature properties of Nb-Zr-c ternary alloys. *Mater Sci Eng, A* 341(1–2):282–288
- [2] Al-Aqeeli N, Hussein M, Suryanarayana C (2015) Phase evolution during high energy ball milling of immiscible Nb-Zr alloys. *Adv Powder Technol* 26(2):385–391
- [3] Hussein MA, Suryanarayana C, Arumugam M, Al-Aqeeli N (2015) Effect of sintering parameters on microstructure, mechanical properties and electrochemical behavior of Nb-Zr alloy for biomedical applications. *Mater Design* 83:344–351
- [4] Banerjee S, Mukhopadhyay P (2010) Phase transformations: examples from titanium and zirconium alloys. Elsevier, USA
- [5] Perovic A, Weatherly G (1997) The promonotectoid region of the Nb-Zr system. *J Phase Equilib* 18(3):245
- [6] Toda Y, Nakagawa H, Koyama T, Miyazaki T (1998) An analysis of the phase decomposition in Nb-Zr alloy based on the system free energy theory. *Mater Sci Eng, A* 255(1–2):90–97
- [7] Porter DA, Easterling KE (2009) Phase transformations in metals and alloys (revised reprint). CRC Press, UK
- [8] Cahn JW (1961) On spinodal decomposition. *Acta Metall* 9(9):795–801
- [9] Khachaturyan AG (2013) Theory of structural transformations in solids. Courier Corporation, USA
- [10] Furuhashi T, Makino T, Idei Y, Ishigaki H, Takada A, Maki T (1998) Morphology and crystallography of  $\alpha$  precipitates in  $\beta$  ti-mo binary alloys. *Mater Trans, JIM* 39(1):31–39
- [11] Devaraj A, Nag S, Banerjee R (2013) Alpha phase precipitation from phase-separated beta phase in a model ti-mo-al alloy studied by direct coupling of transmission electron microscopy and atom probe tomography. *Scripta Mater* 69(7):513–516
- [12] Choudhuri D, Zheng Y, Alam T, Shi R, Hendrickson M, Banerjee S, Wang Y, Srinivasan S, Fraser H, Banerjee R (2017) Coupled experimental and computational investigation of omega phase evolution in a high misfit titanium-vanadium alloy. *Acta Mater* 130:215–228
- [13] Choudhuri D, Srinivasan SG, Gibson MA, Zheng Y, Jaeger DL, Fraser HL, Banerjee R (2017) Exceptional increase in the creep life of magnesium rare-earth alloys due to localized bond stiffening. *Nat Commun* 8(1):1–9
- [14] Choudhuri D, Gwalani B, Gorsse S, Komarasamy M, Mantri SA, Srinivasan SG, Mishra RS, Banerjee R (2019) Enhancing strength and strain hardenability via deformation twinning in fcc-based high entropy alloys reinforced with intermetallic compounds. *Acta Mater* 165:420–430
- [15] Choudhuri D, Matteson S, Knox R (2021) Nucleation of coupled body-centered-cubic and closed-packed structures in liquid ni-cr alloys. *Scripta Mater* 199:113857
- [16] Choudhuri D, Majumdar BS, Wilkinson H (2022) Investigation of in-liquid ordering mediated transformations in al-sc via ab initio molecular dynamics and unsupervised learning. *Phys Rev Mater* 6(10):103406
- [17] Anderson PM, Hirth JP, Lothe J (2017) Theory of dislocations. Cambridge University Press, Cambridge
- [18] Bian J, Yang L, Niu X, Wang G (2018) Orientation-dependent deformation mechanisms of bcc niobium nanoparticles. *Phil Mag* 98(20):1848–1864
- [19] Gröger R, Chlup Z, Kuběnová T, Kuběna I (2019) Interplay of slip and twinning in niobium single crystals compressed at 77 k. *J Mater Res* 34(2):261–270
- [20] Singh D, Sharma P, Jindal S, Kumar P, Kumar P, Parashar A (2019) Atomistic simulations to study crack tip

- behaviour in single crystal of bcc niobium and hcp zirconium. *Curr Appl Phys* 19(1):37–43
- [21] Zotov N, Grabowski B (2021) Molecular dynamics simulations of screw dislocation mobility in bcc Nb. *Modell Simul Mater Sci Eng* 29(8):085007
- [22] Li P, Huang Y, Wang K, Xiao S, Wang L, Yao S, Zhu W, Hu W (2022) Crystallographic-orientation-dependence plasticity of niobium under shock compressions. *Int J Plast* 150:103195
- [23] Pink E, Arsenault RJ (1980) Low-temperature softening in body-centered cubic alloys. *Prog Mater Sci* 24:1–50
- [24] Trinkle DR, Woodward C (2005) The chemistry of deformation: how solutes soften pure metals. *Science* 310(5754):1665–1667
- [25] Hu Y-J, Fellingner MR, Butler BG, Wang Y, Darling KA, Keeskes LJ, Trinkle DR, Liu Z-K (2017) Solute-induced solid-solution softening and hardening in bcc tungsten. *Acta Mater* 141:304–316
- [26] Chatterjee P, Pabi S, Manna I (1999) An allotropic transformation induced by mechanical alloying. *J Appl Phys* 86(10):5912–5914
- [27] Chattopadhyay P, Pabi S, Manna I (2001) A metastable allotropic transformation in Nb induced by planetary ball milling. *Mater Sci Eng, A* 304:424–428
- [28] Wang Q, Wang J, Li J, Zhang Z, Mao SX (2018) Consecutive crystallographic reorientations and superplasticity in body-centered cubic niobium nanowires. *Sci Adv* 4(7):eaas8850
- [29] Li X, Wang Q, Fan J, Wang Y, Zhang Z, Wang J (2022) Shock-induced  $\alpha''$  martensitic transformation in Nb single crystals. *Mater Sci Eng, A* 846:143274
- [30] Luo W, Roundy D, Cohen ML, Morris J Jr (2002) Ideal strength of bcc molybdenum and niobium. *Phys Rev B* 66(9):094110
- [31] Plimpton SJ (1995) Fast parallel algorithms for short-range molecular dynamics. *J Comput Phys* 117(3):1–19
- [32] Thompson AP, Plimpton SJ, Mattson W (2009) General formulation of pressure and stress tensor for arbitrary many-body interaction potentials under periodic boundary conditions. *J Chem Phys* 131(15):154107
- [33] Starikov S, Smirnova D (2021) Optimized interatomic potential for atomistic simulation of Zr-Nb alloy. *Comput Mater Sci* 197:110581
- [34] Smirnova D, Starikov S (2017) An interatomic potential for simulation of Zr-Nb system. *Comput Mater Sci* 129:259–272
- [35] Abriata J, Bolcich J (1982) The Nb- Zr (niobium- zirconium) system. *J Phase Equilib* 3(1):34–44
- [36] Jin O, Zhang Z, Liu B (1995) Alloying behavior induced by ion mixing in a system with positive heat of formation. *J Appl Phys* 78(1):149–154
- [37] Banerjee R, Collins PC, Fraser HL (2002) Phase evolution in laser-deposited titanium-chromium alloys. *Metall Mater Trans* 33(7):2129
- [38] Straumal BB, Gornakova AS, Fabricznaya OB, Kriegel MJ, Mazilkin AA, Baretzky B, Gusak A, Dobatkin S (2012) Effective temperature of high pressure torsion in Zr-Nb alloys. *High Temp Mater Processes (London)* 31(4–5):339–350
- [39] Sun Y, Li K, Gao B, Sun P, Fu H, Liu Z, Yin J (2020) Study on microstructure and wear resistance of Zr-17nb alloy irradiated by high current pulsed electron beam. *Rev Adv Mater Sci* 59(1):514–522
- [40] Hirel P (2015) AtomsK: a tool for manipulating and converting atomic data files. *Comput Phys Commun* 197:212–219. <https://doi.org/10.1016/j.cpc.2015.07.012>
- [41] Qi Y, Strachan A, Cagin T, Goddard WA III (2001) *Mater Sci Eng, A* 309:156–159
- [42] Frenkel D, Smit B, Ratner MA (1996) *Understanding molecular simulation: from algorithms to applications, vol 2*. Academic press San Diego, USA
- [43] Allen MP, Tildesley DJ (2017) *Computer simulation of liquids*. Oxford University Press, UK
- [44] Tuckerman M (2010) *Statistical mechanics: theory and molecular simulation*. Oxford University Press, UK
- [45] Wang L, Hoyt JJ (2021) Layering misalignment and negative temperature dependence of interfacial free energy of b2-liquid interfaces in a glass forming system. *Acta Mater* 219:117259
- [46] Stukowski A (2010) Visualization and analysis of atomistic simulation data with OVITO-the Open Visualization Tool. *Modell Simul Mater Sci Eng* 18(1):015012. <https://doi.org/10.1088/0965-0393/18/1/015012>
- [47] Stukowski A, Albe K (2010) Extracting dislocations and non-dislocation crystal defects from atomistic simulation data. *Modell Simul Mater Sci Eng* 18(8):085001. <https://doi.org/10.1088/0965-0393/18/8/085001>
- [48] Stukowski A (2010) Fast parallel algorithms for short-range molecular dynamics. *Modell Simul Mater Sci Eng* 18(3):015012–015018
- [49] Stukowski A, Bulatov VV, Arsenlis A (2012) Automated identification and indexing of dislocations in crystal interfaces. *Modell Simul Mater Sci Eng* 20(8):085007
- [50] Stukowski A (2012) Structure identification methods for atomistic simulations of crystalline materials. *Modell Simul Mater Sci Eng* 20(4):045021

- [51] Larsen PM, Schmidt S, Schiøtz J (2016) Robust structural identification via polyhedral template matching. *Modell Simul Mater Sci Eng* 24(5):055007
- [52] Shimizu F, Ogata S, Li J (2007) Theory of shear banding in metallic glasses and molecular dynamics calculations. *Mater Trans* 48(11):2923–2927. <https://doi.org/10.2320/matertrans.MJ200769>
- [53] Choudhuri D, Srinivasan SG, Mishra RS (2020) Deformation of lamellar fcc-b2 nanostructures containing kurdjumov-sachs interfaces: relation between interfacial structure and plasticity. *Int J Plast* 125:191–209
- [54] Choudhuri D, CampBell A (2020) Interface dominated deformation mechanisms in two-phase fcc/b2 nanostructures: Nishiyama-wasserman vs. kurdjumov-sachs interfaces. *Comput Mater Sci* 177:109577
- [55] Choudhuri D, Majumdar BS (2020) Structural changes during crystallization and vitrification of dilute fcc-based binary alloys. *Materialia* 12:100816
- [56] Wang Y, Zhang D, Pi Z, Lin J, Wen C (2019) Phase field simulation of spinodal decomposition in Zr-Nb alloys for implant materials. *J Appl Phys* 126(8):085102
- [57] Kocks U, Mecking H (2003) Physics and phenomenology of strain hardening: the fcc case. *Prog Mater Sci* 48(3):171–273
- [58] Mantri S, Choudhuri D, Behera A, Cotton J, Kumar N, Banerjee R (2015) Influence of fine-scale alpha precipitation on the mechanical properties of the beta titanium alloy beta-21s. *Metall and Mater Trans A* 46:2803–2808
- [59] Kosterz G, Cahn R, Haasen P (1983) *Physical metallurgy*, In: RW Cahn and P. Haasen (Eds.), Elsevier, Amsterdam, 793
- [60] Kolmogorov AN (1937) On the statistical theory of the crystallization of metals. *Bull Acad Sci USSR, Math Ser* 1(3):355–359
- [61] Malvern LE (1969) *Introduction to the mechanics of a continuous medium*, no. Monograph
- [62] Dieter GE, Bacon D (1976) *Mechanical metallurgy*, vol 3. McGraw-hill New York, New York

**Publisher's Note** Springer Nature remains neutral with regard to jurisdictional claims in published maps and institutional affiliations.